

# A New Solution for Camera Calibration and Real-Time Image Distortion Correction in Medical Endoscopy - Initial Technical Evaluation

Rui Melo, João P. Barreto, *Member, IEEE*, and Gabriel Falcão, *Member, IEEE*,

**Abstract**—Medical endoscopy is used in a wide variety of diagnostic and surgical procedures. These procedures are renowned for the difficulty of orienting the camera and instruments inside the human body cavities. The small size of the lens causes radial distortion of the image, which hinders the navigation process and leads to errors in depth perception and object morphology. This article presents a complete software-based system to calibrate and correct the radial distortion in clinical endoscopy in real time. Our system can be used with any type of medical endoscopic technology, including oblique-viewing endoscopes and HD image acquisition. The initial camera calibration is performed in an unsupervised manner from a single checkerboard pattern image. For oblique-viewing endoscopes the changes in calibration during operation are handled by a new adaptive camera projection model and an algorithm that infer the rotation of the probe lens using only image information. The workload is distributed across the CPU and GPU through an optimized CPU+GPU hybrid solution. This enables real-time performance, even for HD video inputs. The system is evaluated for different technical aspects, including accuracy of modeling and calibration, overall robustness and runtime profile. The contributions are highly relevant for applications in computer aided surgery and image guided intervention such as improved visualization by image warping, 3D modeling, and visual SLAM.

**Index Terms**—Medical Endoscopy, Radial Distortion, GPU, Camera Model, Camera Calibration, Exchangeable Optics.

## I. INTRODUCTION

**R**IGID medical endoscopes typically combine an endoscopic lens with a Charge-Coupled Device (CCD) camera, as shown in Fig.1(a). The lens covers the CCD sensor that acquires images with the dark aperture (circular region) being visible due to the optics converter used for mounting the lens on the camera (Fig.1(b)). Two types of rigid endoscopes are commonly used in medicine: the *forward viewing endoscopes*, where the optical axis is aligned with the cylindrical probe, and the *oblique viewing endoscopes*, where the optical axis makes an angle of  $30^\circ$  or  $70^\circ$  with respect to the symmetry axis of the probe. The viewing direction of the latter can be changed without moving the camera head by simply rotating the endoscope around its symmetry axis [1]–[3]. This rotation is typically inferred by observing the position of a triangular mark on the periphery of the circular

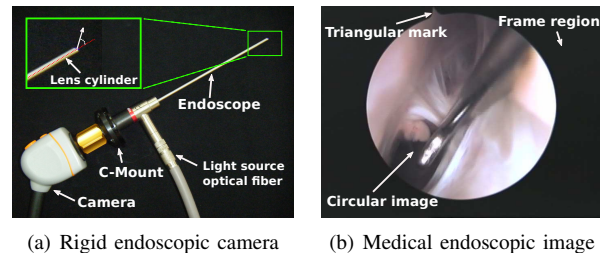


Fig. 1. The rigid endoscope combines a lens with a CCD camera (a). The system enables the visualization of human body cavities whose access is difficult or limited, and is widely used for both surgery and diagnosis. (b) is an image of the interior of a knee joint, acquired by the  $30^\circ$  oblique viewing arthroscopy, which is used in the experiments throughout the article.

region (Fig.1(b)). Oblique viewing endoscopes are specially useful in inspecting narrow cavities, such as the articulations (arthroscopy) or the sinus (rhinoscopy), where the space to maneuver the probe is very limited.

Endoscopic video is often the only guidance for the medical practitioner during minimally invasive procedures. Navigation inside the human body is achieved by recognizing local anatomical landmarks from close range images, and the execution of tasks requires unnatural hand-eye coordination that is only mastered after a long training period. The manufacturers of endoscopic equipment try to mitigate these difficulties by working to improving the imaging conditions. In recent years the introduction of better camera technologies (e.g. High-Definition (HD) and 3 CCD sensors for improved image and color resolution) and the development of new optics and lenses (e.g. increased depth of field, anti-fog effect) have considerably improved visual perception for the medical practitioner.

Despite all these developments, strong Radial Distortion (RD) is a problem that persists because of the small size of the lenses. The distortion causes a nonlinear geometric deformation of the image, with the points being moved radially towards the center [4]. Fig.2(a) shows an endoscopic image of a planar checkerboard pattern. RD can be easily recognized because straight lines are projected into curves in the image periphery. It can also be observed that strong distortion severely affects the perception of relative size and depth, and the user is hardly able to tell that the imaged scene is planar [5], [6]. This issue has recently begun to merit the attention of the manufacturers and last year Striker<sup>®</sup> announced the first laparoscopy system with reduced RD. The distortion is diminished by combining a novel optical design with cropping of the image periphery where RD is more noticeable. Unfortunately, the images

The authors are with the Dept. of Electrical and Computer Engineering, Faculty of Science and Technology, University of Coimbra, Portugal. Rui Melo and João Barreto are affiliated with the Institute for Systems and Robotics, and Gabriel Falcão is with the Instituto de Telecomunicações.

This article has supplementary downloadable material available at <http://ieeexplore.ieee.org>. The material includes a multimedia movie clip that shows the system stages running in real-time.

are far from being geometrically correct perspectives, the cropping decreases the effective Field of View (FOV), and the solution can neither be extended to small diameter lenses (e.g. arthroscopy, rhinoscopy, etc), nor to legacy systems using Standard-Definition (SD) image acquisition and display.

Given the small size of the lenses, it is unlikely that improvements in optical design will ever definitively solve the RD issue. An alternative is to model the lens distortion and correct the acquired frames using image warping. This is a software based solution that has important advantages: (i) it renders geometrically correct perspective images, provided that the RD is correctly modeled and quantified; (ii) it is flexible in that it can be applied to any type of endoscopic equipment, regardless of the lens diameter or the image acquisition technology; and (iii) it is a very cost-effective solution, as long as the computation uses Commercial, Off-the-Shelf (COTS) hardware. Despite these potential advantages, RD correction by image warping is not a reality because of the following issues:

- *Camera calibration in the Operating Room (OR):* Distortion compensation requires modeling the camera projection, and estimating the corresponding parameters. An endoscope cannot be calibrated in advance by the manufacturer because it has exchangeable optics that are usually assembled in the OR before the procedure. Therefore, and since the calibration must be done by the medical practitioner, the procedure must be robust and automatic so that a non-expert user can execute it quickly.
- *Changes in the calibration due to lens rotation:* In oblique viewing endoscopes the motion between optics and camera sensor changes the projection parameters and the position and shape of the circular boundary separating the two image regions [7]. Since it is not feasible to calibrate the endoscope for every possible lens position, the calibration parameters must be updated according to a camera model that accounts for this relative motion.
- *Execution in real-time:* All the computations, including the rendering of the corrected images, must be done in real time. This is specially problematic in the case of HD systems providing a high frame resolution.

This article addresses the above issues and presents a fully functional software-based system for calibrating and improving visualization in medical endoscopy by correcting the image radial distortion. The solution runs in real time on a standard computer with a COTS Graphics Processing Unit (GPU), and no further equipment or instrumentation is required. Moreover, it can be potentially used in any type of medical endoscopy, regardless of the type (forward-viewing or oblique-viewing), or the image acquisition technology (SD or HD). User intervention is limited to the acquisition of a single calibration frame at the beginning of the clinical procedure.

Throughout the article, the experimental evaluations are carried using a 4-mm arthroscope with a lens cut of  $30^\circ$  that is mounted in a CCD camera with resolution 1280x960. We do not consider the situation where the endoscopic probe suffers mechanical torsion. This causes transitory changes in the projection model [7] that do not affect the practical

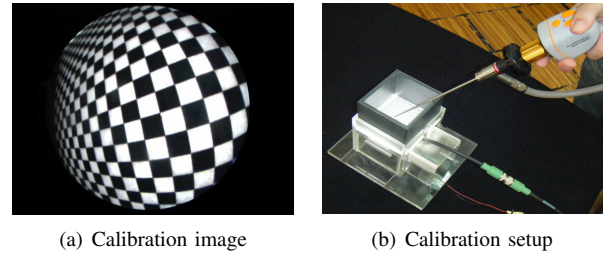


Fig. 2. Calibration of the endoscopic camera from a single image of a planar checkerboard pattern. The calibration image of (a) is acquired in an unconstrained manner using the setup shown in (b). The setup consists of a  $10 \times 10$ cm acrylic box with a checkerboard pattern inside that is backlit uniformly using a NERLITE<sup>®</sup> back-light of 350mA.

usefulness of the proposed system.

### A. Notation

Vectors and vector functions are represented by bold symbols, e.g.  $\mathbf{x}$ ,  $\mathbf{F}(\mathbf{x})$ , scalars and scalar functions are indicated by plain letters, e.g.  $r$ ,  $f(\mathbf{x})$ ,  $g(r)$ , matrices and image signals are respectively denoted by capital letters in sans serif and typewriter fonts, e.g. the matrix  $M$  and the image  $I$ . Points in the plane are typically represented using homogeneous coordinates, with the symbol  $\sim$  denoting the equality up to scale, e.g.  $\mathbf{x} \sim (x_1 \ x_2 \ 1)^T$ .  $I_m$  indicates the  $m \times m$  identity matrix, while  $0_{m \times n}$  denotes a rectangular matrix with zeros. Conic curves in the projective plane are represented by a  $3 \times 3$  symmetric matrix, e.g.  $\Omega$ . If a matrix  $R$  is a function of a scalar  $\alpha$  and/or a vector  $\mathbf{q}$ , then the input parameters are indicated in subscript, e.g.  $R_{\alpha, \mathbf{q}}$ .

## II. SYSTEM OVERVIEW AND RELATED WORK

We propose a complete solution for RD correction in medical endoscopy that comprises the modules and blocks shown in the scheme in Fig.3. The medical practitioner starts by acquiring a single image of a checkerboard pattern using the setup in Fig.2. The corners in the calibration frame are detected automatically, and both the matrix of intrinsic parameters  $K_0$  and the radial distortion  $\xi$  are estimated without further user intervention. After this brief initialization step the processing pipeline on the right of Fig.3 is executed for each acquired image. At each frame time instant  $i$  we detect the boundary contour  $\Omega_i$ , as well as the position of the triangular mark  $\mathbf{p}_i$ . The detection results are used as input in an Extended Kalman Filter (EKF) which, given the boundary  $\Omega_0$  and marker position  $\mathbf{p}_0$  in the calibration frame, then estimates the relative image rotation due to the the lens probe rotation with respect to the camera head. This 2D rotation is parametrized by the angle  $\alpha_i$  and the fixed point  $\mathbf{q}_i$  that serve as input for updating the camera calibration based on a new adaptive projection model. Finally, the current geometric calibration  $K_i$ ,  $\xi$  is used for warping the input frame and correct the radial distortion. This processing pipeline runs in real time with computationally intensive tasks, like the image warping and the boundary detection, being efficiently implemented using the parallel execution capabilities of the GPU. This section briefly introduces the system building blocks, discusses related work, and emphasizes the new contributions.

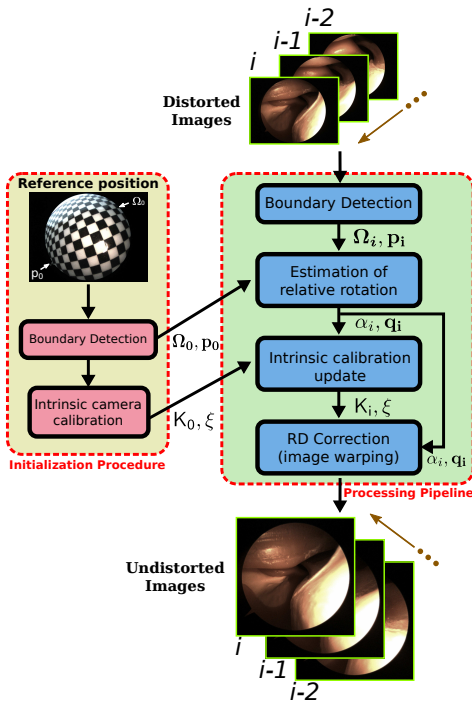


Fig. 3. Scheme showing the different modules of the system that is proposed for correcting the radial distortion of the image. The left-hand side concerns the *Initialization Procedure* that is performed only once, after assembling the endoscopic lens with the CCD camera. The right-hand side shows the *Processing Pipeline* that is executed at each frame time instant  $i$ .

#### A. Boundary Detection

Finding the image contour that separates circular and frame regions is important not only to delimit meaningful visual contents, but also to infer the rotation of the lens probe with respect to the camera head. Section III presents a new algorithm for tracking the boundary contour and the triangular mark across successive frames. The proposed approach is related to work by Fukuda et al. [3] and Stehle et al. [8]. The first infers the lens rotation in oblique viewing endoscopes by extracting the triangular mark using conventional image processing techniques. The method assumes that the position of the circular region does not change during operation, which is in general not true, and it is unclear if it can run in real time. Stehle et al. proposes tracking the boundary contour across frames by fitting a conic curve to edge points detected in radial directions. The main difference from our algorithm is that we use a hybrid CPU+GPU implementation for rendering a polar image and carry out the search along horizontal lines. As discussed in III, this strategy makes it possible to reconcile robustness and accuracy with low computational cost.

#### B. Intrinsic Camera Calibration

The *Initialization Procedure* aims at determining the intrinsic calibration matrix  $K_0$  and the radial distortion  $\xi$  when the lens probe is at a reference position  $\Omega_0, \mathbf{p}_0$ . Planar regular patterns are widely used as a calibration object because they are readily available and simplify the problem of establishing point correspondences. Bouguets toolbox [9] is a popular software that implements Zhang's method [10] for

calibrating a generic camera from a minimum of 3 images of a checkerboard. Unfortunately, the Bouguet toolbox does not meet the usability requirements of our application. In practice the number of input images for achieving accurate results is way above 3, and the detection of grid corners in images with RD needs substantial user intervention. Several authors addressed the specific problem of intrinsic calibration or RD correction in medical endoscopes [5], [6], [11]–[14]. However, these methods are either impractical for use in the OR, or they employ circular dot patterns to enable the automatic detection of calibration points, undermining the results accuracy [15].

Our system reconciles estimation accuracy with usability requirements by using the recent algorithm by Barreto *et al.* that fully calibrates a camera with lens distortion from a single image of a known checkerboard pattern [16]. The intervention of the medical practitioner is limited to the acquisition of a calibration frame from arbitrary position using the setup of Fig.2(b). The purpose of the calibration box is controlling the light conditions for assuring robust automatic detection of grid image corners. Section IV introduces the camera projection model that will be assumed throughout the article, with the interested reader being referred to our previous publication [16] for details about the intrinsic calibration method.

#### C. Estimation of Relative Rotation and Calibration Update

Rigid endoscopes with exchangeable optics allow rotation of the lens scope with respect to the camera-head, which enables observing the walls of narrow cavities without having to displace the camera. The problem is that the relative motion between lens and camera head causes changes in the calibration parameters that prevent the use of a constant model for correcting the distortion [7]. There is a handful of works proposing solutions for this problem [1]–[3], [8], [17], but most of them have the drawback of requiring additional instrumentation for determining the lens rotation [1], [2], [17]. The few methods relying only on image information for inferring the relative motion either lack robustness [3] or are unable to update the full set of camera parameters [8].

Section V proposes a new intrinsic camera model for endoscopes with exchangeable optics that is driven simultaneously by experiment and by the conceptual understanding of the lens arrangement. The parameters of the lens rotation required to update the camera model are estimated by a robust EKF that receives image information about the boundary contour and triangular mark as input. Our dynamic calibration scheme has two important advantages with respect to [8]: (i) the entire projection model is updated as a function of the lens rotation, and not only the RD profile curve; and (ii) the rotation of the lens can still be estimated in the absence of the triangular mark (see Fig.1(b)). The approach is validated by convincing experimental results in reprojecting 3D points in the scene.

#### D. RD Correction using an Hybrid CPU+GPU Solution

Section VI concerns the rendering of correct perspective frames by warping the endoscopic images. The required mapping functions are derived and several visualization aspects are discussed (e.g. resolution, image size). We also present

examples that illustrate the benefits of RD correction in scene perception, and the importance of taking the lens rotation into account. Finally, section VII shows that a CPU solution for carrying out the computation fails to deliver real-time performance. Thus, we propose a hybrid CPU+GPU solution with coalesced memory accesses that enables speedups between 50 and 200 depending on the image resolution. We perform a detailed time profiling of the processing pipeline, showing that the system can correct HD images with an acquisition rate above 25 fps (please see the supplementary video).

### III. ROBUST REAL-TIME DETECTION OF THE BOUNDARY CONTOUR AND TRIANGULAR MARK

This section discusses the localization of the image contour that separates the circular and frame regions (see Fig.1(b)). Since the lens probe moves with respect to the camera head the contour position changes across frames, which prevents using an initial off-line estimation. The boundary detection must be performed at each frame time instant, which imposes constraints on the computational complexity of the chosen algorithm. Several issues preclude the use of naive approaches for segmenting the circular region [18]: the light often spreads to the frame region (Fig.4(a)); the circular region can have dark areas, depending on the imaged scene and lighting conditions (Fig.4(b)); and there are often highlights, specularity, and saturation that affect the segmentation performance (Fig.4(c)).

#### A. Tracking the Boundary Contour across Frames

It is reasonable to assume that the curve to be determined is always an ellipse  $\Omega$  with 5 degrees of freedom (DOF) [4]. Thus, we propose to track the boundary across frames using this shape prior to achieve robustness and quasi-deterministic runtime. Let  $\Omega_{i-1}$  be the curve estimate at the frame time instant  $i-1$  as shown in Fig.5(a). The boundary contour for the current frame  $i$  is updated as follows:

- 1) Consider a set of equally spaced lines  $\mathbf{r}_j$ , with  $j = 1, 2, \dots, N$ , that intersect in the conic center  $\mathbf{w}_{i-1}$  (this center can be easily computed by selecting the third column of the adjoint of the  $3 \times 3$  matrix  $\Omega_{i-1}$  [4]).
- 2) For each  $\mathbf{r}_j$ , interpolate the image signal and compute the 1-D directional derivative at every point location.
- 3) For each  $\mathbf{r}_j$  choose the first maximum of the 1-D derivative when moving from the periphery towards the center. The detected point  $\mathbf{s}_j$  is the probable location where the scan line  $\mathbf{r}_j$  intersects the boundary contour.
- 4) Compute  $\Omega_i$  by fitting an ellipse to the  $N$  points  $\mathbf{s}_j$  using a standard RANdom SAMple Consensus (RANSAC) procedure [19], [20].

This tracking approach is robust provided that the number of radial scan directions is high enough to handle possible outlier detections. Unfortunately, the computational effort is proportional to the value of  $N$ , making difficult to reconcile robustness with strict time requirements<sup>1</sup>. We tackle this by using a hybrid CPU+GPU implementation where the image

<sup>1</sup>In our experiments, we use  $N = 180$  for input image resolutions of  $640 \times 480$  and  $N = 1000$  for resolutions of  $2448 \times 2048$ .

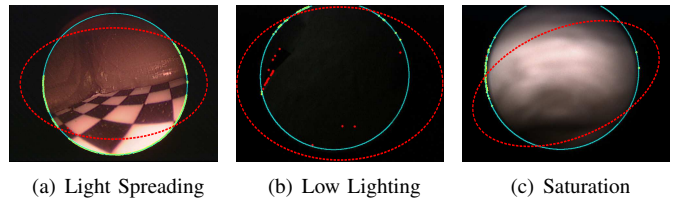


Fig. 4. Boundary detection in extreme situations. The dashed and solid overlays are respectively the initialization and the final contour. The algorithm converges in 3 to 5 iterations depending on the initial estimate.

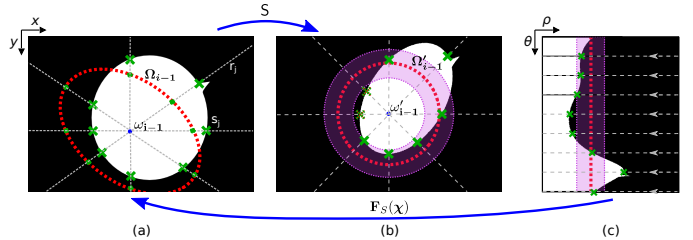


Fig. 5. Tracking of the boundary contour. The schemes from left to the right relate to the original frame acquired at time instant  $i$ , the warped image using the affine transformation  $S$ , and the polar image obtained by changing from Cartesian to spherical coordinates. The red dashed overlay relates to the previous boundary estimate, and the crosses are the detected points in the current contour.  $S$  maps  $\Omega_{i-1}$  into a unit circle. The purple shaded area is the image region that suffers the polar warp and is where the search is performed.

interpolation is carried out in the parallel pipeline of the GPU. As shown in Fig.5, instead of working in the radial directions we propose to unfold the image according to a polar map, and carry out the edge detection in the horizontal directions. The warping operation can be performed quickly in the GPU and the topological change in the image domain significantly simplifies both the computation of the 1D-derivatives and the subsequent detection of the contour points  $\mathbf{s}_j$ .

To implement this strategy we must derive the mapping function that transforms the current frame  $i$ , shown in Fig.5(a), into the polar image of Fig.5(c). Let  $\Omega_{i-1}$  be the estimation of the boundary contour in the frame  $i-1$ . It is well known that there is always an affine transformation that maps an arbitrary ellipse into a unitary circle whose center is in the origin [4]. Such transformation  $S$  is given by

$$S \sim \begin{pmatrix} r \cos(\phi) & r \sin(\phi) & -r(w_{i-1,x} \cos(\phi) + w_{i-1,y} \sin(\phi)) \\ -\sin(\phi) & \cos(\phi) & w_{i-1,x} \sin(\phi) - w_{i-1,y} \cos(\phi) \\ 0 & 0 & 1 \end{pmatrix}, \quad (1)$$

where  $r$  is the ratio between the minor and major axis of  $\Omega_{i-1}$ ,  $\phi$  is the angle between the major axis and the horizontal direction, and  $(w_{i-1,x}, w_{i-1,y})$  are the non-homogeneous coordinates of the conic center  $\mathbf{w}_{i-1}$ . The transformation  $S$  is used to generate the intermediate result of Fig.5(b), and the polar image (Fig.5(c)) is obtained by applying a change from Cartesian to spherical coordinates.

The edge points are detected by scanning the horizontal lines of Fig.5(c) from the right to the left. These points, which are expressed in spherical coordinates  $\chi = (\rho, \theta)$ , are mapped back into the original image points by the function  $F_S$  of equation 2. The current conic boundary  $\Omega_i$  is finally estimated using the robust conic fitting that avoids the pernicious effects

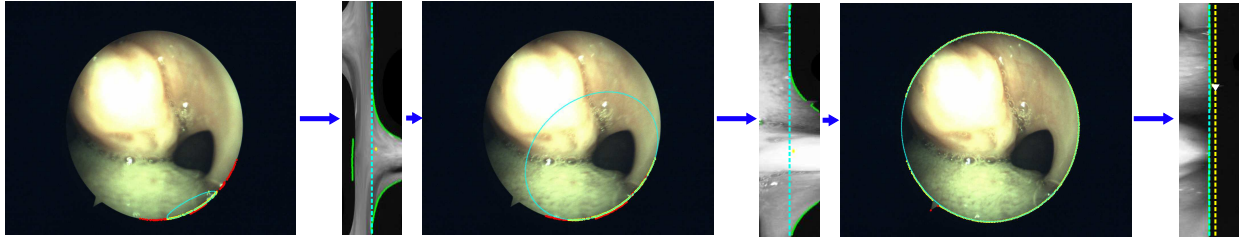


Fig. 6. Convergence of the boundary contour estimation after a poor initialization. We show from left to right a sequence of 3 successive frames (15 fps) of the oral cavity, with the rendered polar images in between. The green dots in the polar images are the point detections that are mapped back into the original image using  $\mathbf{F}_S$ . The RANSAC procedure divides the points into inliers (yellow dots) and outliers (red dots), and estimates the boundary contour at the current frame time instant. Note that after convergence the boundary is mapped into the middle vertical line of the polar image (cyan dashed overlay) and the triangular mark can be easily detected (white triangle in the last polar image) by scanning the vertical dashed yellow line for the maximum pixel value.

of possible outliers.

$$\mathbf{x} \sim \mathbf{F}_S(\boldsymbol{\chi}) \sim \mathbf{S}^{-1} \begin{pmatrix} \rho \cos(\theta) \\ \rho \sin(\theta) \\ 1 \end{pmatrix}, \quad (2)$$

Fig.6 shows the tracking behavior in a sequence of 3 frames when the initial boundary estimate is significantly off. After correct convergence the boundary contour is mapped into the central vertical line of the polar image enabling the robust detection of the triangular lens mark. As shown in the right-hand side of Fig.6, we scan an auxiliary vertical line slightly deviated to the right, and select the pixel location that has maximum intensity. It is also important to note that the search for contour points is limited to a ring region around the previous boundary estimation (Fig.5(b)), saving computational time both in the polar warping and in the horizontal line scanning (Fig.5(c)). The CPU+GPU hybrid implementation of the boundary tracking allows the computationally efficient reconciliation of robustness and accuracy. As we shall see in section VII, the detection of the boundary and lens mark takes between 4 and 13ms depending on the image size.

#### IV. INITIAL INTRINSIC CALIBRATION

This section discusses the initial intrinsic calibration of the endoscopic camera. This is a fully automatic process that uses the Single Image Calibration (SIC) algorithm proposed in [16].

##### A. Projection Model

A camera equipped with a rigid endoscope is a compound system with a complex optical arrangement. The projection is central [7] and the image distortion is described well by the so-called division model [16]. Let  $\mathbf{X}$  be the vector of homogeneous coordinates of a 3D point represented in a world reference frame. Point  $\mathbf{X}$  is projected into point  $\mathbf{x}$  in the endoscopic image such that

$$\mathbf{x} \sim \mathbf{K}_0 \Gamma_\xi(\mathbf{P} \mathbf{X}). \quad (3)$$

$\mathbf{P}$  denotes the standard  $3 \times 4$  projection matrix [4],  $\Gamma_\xi$  is a nonlinear projective function that accounts for the image radial distortion, and  $\mathbf{K}_0$  is the matrix of intrinsic parameters with

the following structure

$$\mathbf{K}_0 \sim \begin{pmatrix} a f & s f & c_x \\ 0 & a^{-1} f & c_y \\ 0 & 0 & 1 \end{pmatrix} \quad (4)$$

where  $f$ ,  $a$ , and  $s$ , stand respectively for the focal length, aspect ratio, and skew, and  $\mathbf{c} = (c_x, c_y)^\top$  are the non-homogeneous coordinates of the image principal point. The image radial distortion is described by the division model [16], with world undistorted projected points  $\mathbf{x}_u \sim (x_u y_u z_u)^\top$  being mapped into world distorted points  $\mathbf{x}_d$  according to:<sup>2</sup>

$$\Gamma_\xi(\mathbf{x}_u) \sim (2x_u \ 2y_u \ z_u + \sqrt{z_u^2 - 4\xi(x_u^2 + y_u^2)})^\top. \quad (5)$$

The amount of nonlinear distortion is quantified by a single scalar parameter  $\xi$  that always takes a non-positive value ( $\xi \leq 0$ ). The mapping in the projective plane  $\mathbb{P}^2$  induced by  $\Gamma_\xi$  is bijective, and the inverse function  $\Gamma_\xi^{-1}$  transforms distorted points  $\mathbf{x}_d \sim (x_d y_d z_d)^\top$  back into undistorted points  $\mathbf{x}_u$  [16]:

$$\Gamma_\xi^{-1}(\mathbf{x}_d) \sim (x_d \ y_d \ z_d^2 + \xi(x_d^2 + y_d^2))^\top. \quad (6)$$

If the distance between  $\mathbf{x}_d$  and the origin  $\mathbf{O} \sim (001)^\top$  is

$$r_d = \sqrt{\frac{x_d^2}{z_d^2} + \frac{y_d^2}{z_d^2}}, \quad (7)$$

then it follows from the inverse mapping of equation 6 that the distance between  $\mathbf{x}_u$  and  $\mathbf{O}$  is

$$r_u = \frac{r_d}{1 + \xi r_d^2}. \quad (8)$$

Henceforth, and without loss of generality, it will be assumed that the 3D point  $\mathbf{X}$  is expressed in the camera reference frame, which means that  $\mathbf{P} \sim \begin{pmatrix} 1 & 0 \\ 0 & 1 \\ 0 & 0 \end{pmatrix}$ .

##### B. Single Image Calibration (SIC) in the OR

We showed in [16] that a camera that follows the projection model described above can be calibrated from a single checkerboard frame taken from an arbitrary position. Thanks to this result it is possible to limit the user intervention in the OR to the acquisition of an image of a planar grid that

<sup>2</sup>Please note that  $\mathbf{x}_d \sim \mathbf{K}_0^{-1} \mathbf{x}$  and that points  $\mathbf{x}_d$  and  $\mathbf{x}_u$  are expressed in a system of coordinates with origin in the distortion center.

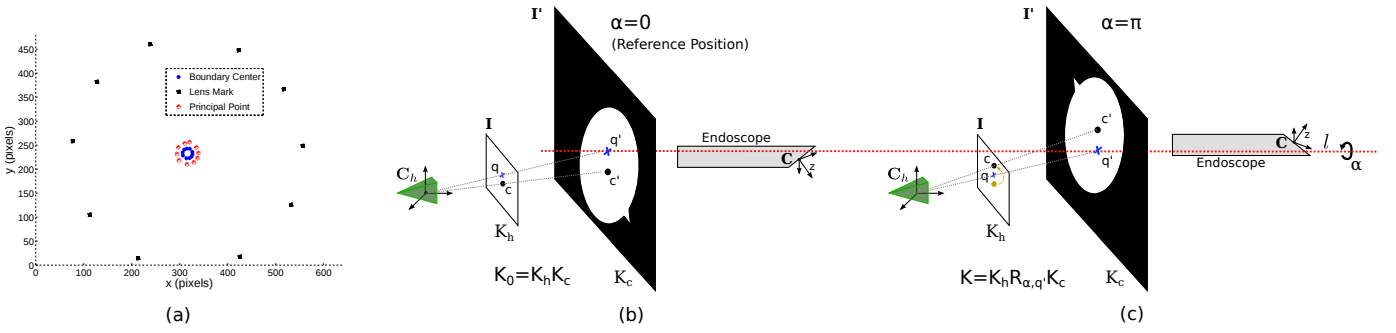


Fig. 7. (a) is a plot of the principal point  $c$ , triangular mark  $p$ , and boundary center  $w$ , when the lens undergoes a full rotation. (b) and (c) illustrates the model and assumptions that are considered for updating the intrinsic matrix of the endoscopic camera. The lens projects a virtual image onto a plane  $I'$  that is imaged into  $I$  by a CCD camera. The relative rotation of the lens is around an axis  $I$  that is parallel to the optical axis and orthogonal to planes  $I$  and  $I'$ .  $c$  represents the principal point and  $q$  is the center of the induced image rotation.

TABLE I  
COMPARISON BETWEEN SIC AND BOUGUET CALIBRATION.

	$c_x$ (px)	$c_y$ (px)	$f$ (mm)	$\xi$
<b>SIC (mean)</b>	595.77	500.14	558.88	-0.527
<b>SIC (std)</b>	7.069	4.889	34.935	0.0066
<b>Hartley (mean)</b>	618.15	522.38	-	-
<b>Hartley (std)</b>	42.96	63.16	-	-
<b>Hartley RANSAC (mean)</b>	599.23	499.99	-	-
<b>Hartley RANSAC (std)</b>	6.8715	7.0680	-	-
<b>Bouguet</b>	599.32	497.08	541.90	-0.497

is backlit to help automatic corner detection in a robust and accurate manner.

Table I compares the calibration results obtained with our SIC algorithm, the non-parametric approach proposed by Hartley and Kang [21], a robust variant of [21] that applies RANSAC for estimating the fundamental matrix that encodes the distortion center, and the Bouguet toolbox [9]. The experiment considers 10 images of the checkerboard pattern with a resolution of  $1280 \times 960$ . The first row shows the mean and standard deviation of the 10 independent calibration results achieved by SIC. The second and third rows refer to the non-parametric approach that, unlike SIC, only recovers the center and discrete points of the distortion profile curve. Finally, the last row shows the results obtained with [9] using the 10 images in simultaneous. Since Bouguet assumes a polynomial model, the estimated distortion profile is fitted with the division model for comparison purposes. It can be observed that SIC exhibits a very good repeatability, and provides mean values for the calibration parameters that are similar to the ones achieved with [9] using all the images in simultaneous. It is also interesting to verify that the distortion center estimation is consistent with the parameter-free approach, which proves that the assumed lens model is appropriated.

## V. MODELING THE EFFECT OF THE LENS ROTATION IN THE INTRINSIC CALIBRATION

The initialization procedure determines the camera calibration  $K_0$ ,  $\xi$  when the lens probe is in a particular angular position, henceforth referred as the *reference position*. As discussed in section II, the relative rotation between lens and camera-head changes the intrinsic calibration in a manner that affects the RD correction by image warping. In order to assess

this effect we acquired 10 calibration images while rotating the lens probe for a full turn. The calibration was estimated for each angular position using the methodology in section IV, and both the boundary  $\Omega$  and the triangular mark were located as described in section III. Fig.7(a) plots the results for the principal point  $c$ , the boundary center  $w$ , and the lens mark  $p$ . Since the three points describe almost perfect concentric trajectories it seems reasonable to model the effect of the lens rotation on the camera intrinsics by means of a rotation around an axis orthogonal to the image plane. This idea has already been advanced by Wu et al. [2], but they consider that the axis always goes through the principal point, an assumption that in general does not hold, as shown by our experiment.

### A. Projection Model that Accounts for the Lens Rotation

The scheme in Fig.7(b) and (c) aims to give the idea of the proposed model for describing the effect of the lens rotation in the intrinsics. Let us assume that the endoscopic lens projects a virtual image onto a plane  $I'$  placed at the far end. We can think of  $I'$  as the image that would be seen by looking directly through the endoscope eye-piece.  $K_c$  is the intrinsic matrix of this virtual projection, and  $c'$  is the point location where the optical axis meets the plane. Now assume that a camera head is connected to the eye-piece, such that the CCD plane  $I$  is perfectly parallel to  $I'$  and orthogonal to the optical axis. The projection onto  $I$  has intrinsics  $K_h$ , with the principal point  $c$  being the image of  $c'$ . So, if the camera is skewless ( $s=0$ ) with square pixels ( $a=1$ ) and  $K_0$  is the intrinsic matrix estimate

$$K_0 \sim \begin{pmatrix} f & 0 & c_x \\ 0 & f & c_y \\ 0 & 0 & 1 \end{pmatrix}, \quad (9)$$

then it can be factorized as

$$K_0 \sim K_h K_c \sim \begin{pmatrix} f_h & 0 & c_x \\ 0 & f_h & c_y \\ 0 & 0 & 1 \end{pmatrix} \begin{pmatrix} f_c & 0 & 0 \\ 0 & f_c & 0 \\ 0 & 0 & 1 \end{pmatrix}, \quad (10)$$

with  $f_c$  being the focal length of the endoscopic lens, and  $f_h$  being the focal length of the camera head that converts metric units into pixels.

Let us now consider that the lens probe is rotated around an axis  $I$  by an angle  $\alpha$  (Fig.7(c)).  $I$  is assumed to be orthogonal to the virtual plane  $I'$ , but not necessarily coincident with the lens axis. In this case the point  $c'$  describes an arc of circle with amplitude  $\alpha$  and, since  $I$  and  $I'$  are parallel, the same happens with its image  $c$ . The intrinsic matrix of the compound optical system formed by the camera head and the rotated endoscope becomes

$$K \sim K_h R_{\alpha, q'} K_c, \quad (11)$$

with  $R_{\alpha, q'}$  being a plane rotation by  $\alpha$  and around the point  $q'$ , where the axis  $I$  intersects  $I'$ .

$$R_{\alpha, q'} = \begin{pmatrix} \cos(\alpha) & \sin(\alpha) & (1-\cos(\alpha))q'_x - \sin(\alpha)q'_y \\ -\sin(\alpha) & \cos(\alpha) & \sin(\alpha)q'_x + (1-\cos(\alpha))q'_y \\ 0 & 0 & 1 \end{pmatrix}, \quad (12)$$

The position of  $q'$  is obviously unchanged by the rotation, and the same is true of its image  $q \sim K_h q'$ . Taking into account the particular structure of  $K_h$ , we can re-write equation 11 in the following manner<sup>3</sup>

$$\begin{aligned} K &\sim R_{\alpha, q} K_h K_c \\ &\sim R_{\alpha, q} K_0 \end{aligned} \quad (13)$$

We have just derived a projection model for the endoscopic camera that accommodates the rotation of the lens probe and is consistent with the observations of Fig.7(a). The initialization procedure estimates the camera calibration  $K_0$ ,  $\xi$  at an arbitrary reference position ( $\alpha=0$ ). At a certain frame time instant  $i$ , the matrix of intrinsic parameters becomes

$$K_i \sim R_{\alpha_i, q_i} K_0, \quad (14)$$

where  $\alpha_i$  is the relative angular displacement of the lens, and  $q_i$  is the image rotation center that remains fixed during the rotation. Since the radial distortion is a characteristic of the lens, the parameter  $\xi$  is unaffected by the relative motion with respect to the camera-head. Thus, from equation 3, it follows that a generic 3D point  $\mathbf{X}$  represented in the camera coordinate frame is imaged at:

$$\mathbf{x} \sim K_i \Gamma_\xi \left( \begin{bmatrix} I_3 & \mathbf{0} \end{bmatrix} \mathbf{X} \right). \quad (15)$$

### B. Rotation Estimation

The update of the intrinsic parameters matrix at each frame time instant requires knowing the relative angular displacement  $\alpha_i$  and the image rotation center  $q_i$ . We now describe how these parameters can be inferred from the position of the boundary contour  $\Omega$  and the triangular mark  $p$ .

Let  $w_i$  and  $w_0$  be respectively the center of the boundary contours  $\Omega_i$  and  $\Omega_0$  in the current and reference frames. Likewise,  $p_i$  and  $p_0$  are the positions of the triangular markers in the two images. We assume that both  $w_i$ ,  $w_0$  and  $p_i$ ,  $p_0$  are related by the plane rotation  $R_{\alpha_i, q_i}$  whose parameters we aim to estimate. This situation is illustrated in Fig.8(a) where it can be easily seen that the rotation center  $q_i$  must be the intersection of the bisectors of the line segments defined by

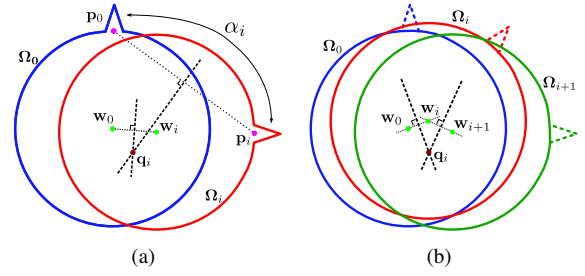


Fig. 8. Computing the image rotation center  $q_i$  when the triangular mark is correctly detected (a), and when there is no mark information (b).

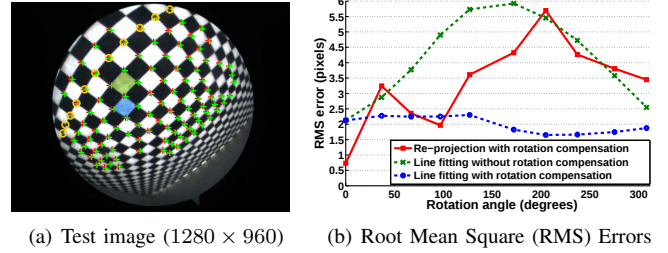


Fig. 9. Experimental validation of the model for updating the camera calibration. The left-hand side shows the image of the planar grid for a lens rotation angle of  $\alpha = 127^\circ$ . The red crosses are the actual position of the image corners, the green crosses refer to the re-projected grid points using the derived model. There is a total of 130 evaluation points, many of which are located in the image periphery where the distortion is more pronounced. The red curve in the graphic of (b) shows the RMS value of the re-projection error for different angular displacements  $\alpha$  of the lens probe. The two other curves refer to the error of fitting a line to a set of collinear points (the yellow circles in Fig 9(a)) after correcting the image distortion with (equation 15) and without (equation 3) taking into account the lens rotation.

$w_i$ ,  $w_0$  and  $p_i$ ,  $p_0$ . Once  $q_i$  is known the estimation of  $\alpha_i$  is trivial. Whenever the triangular mark is unknown (if it does not exist or cannot be detected), the estimation of  $q_i$  requires a minimum of three distinct boundary contours (Fig.8(b)).

In order to avoid under-constrained situations and increase the robustness to errors in measuring  $w$  and  $p$ , we decided to use a stochastic EKF [22] for estimating the rotation parameters. The state transition assumes a constant velocity model for the motion and stationary rotation center. The equation is linear on the state variables, with  $T$  depending on the frame acquisition interval  $\delta t$

$$\begin{pmatrix} \alpha_{i+1} \\ \dot{\alpha}_{i+1} \\ q_{i+1} \end{pmatrix} = \begin{pmatrix} T & 0_{2 \times 3} \\ 0_{3 \times 2} & I_3 \end{pmatrix} \begin{pmatrix} \alpha_i \\ \dot{\alpha}_i \\ q_i \end{pmatrix} \quad T = \begin{pmatrix} 1 & \delta t \\ 0 & 1 \end{pmatrix}. \quad (16)$$

The measurement equation is nonlinear in  $\alpha_i$  and  $q_i$

$$\begin{pmatrix} w_i \\ p_i \end{pmatrix} = \begin{pmatrix} R_{\alpha_i, q_i} & 0_{3 \times 3} \\ 0_{3 \times 3} & R_{\alpha_i, q_i} \end{pmatrix} \begin{pmatrix} w_0 \\ p_0 \end{pmatrix}, \quad (17)$$

with the two last equations being discarded whenever the detection of the triangular mark fails.

### C. Experimental Validation

The proposed model was validated by re-projecting grid corners onto images of the checkerboard pattern acquired for different angles  $\alpha$  (Fig.9). The SIC was performed for the

<sup>3</sup>The assumption of square pixels and zero skew is valid for most CCD cameras. If  $a \neq 1$  or  $s \neq 0$ , then equations 11 and 13 are no longer strictly equivalent. However, the latter is typically a good approximation of the former, and the consequences in terms of modeling accuracy are negligible.

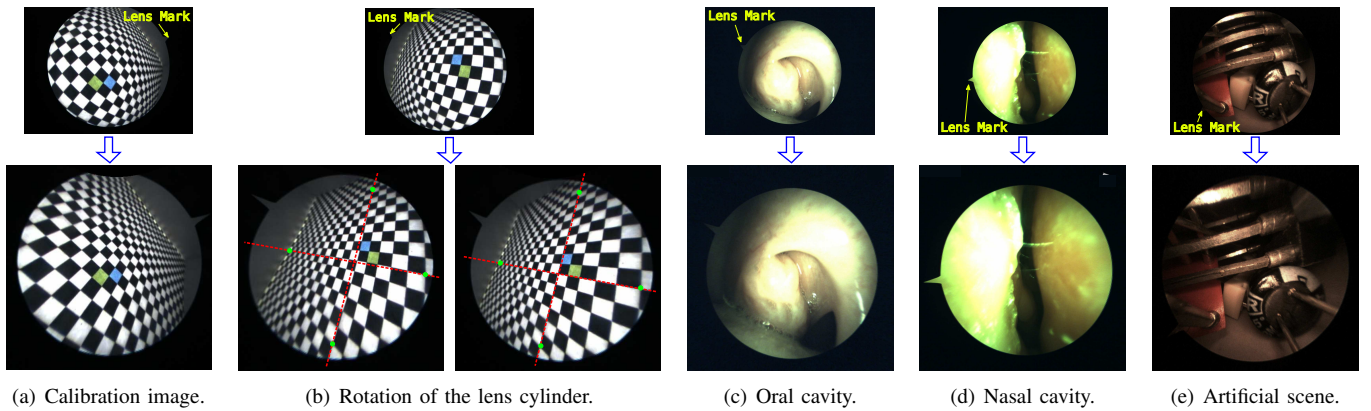


Fig. 10. Radial distortion correction of endoscopic video sequences with lens probe rotation. The original and warped frames are presented in the top and bottom rows, respectively. (a) shows the reference position ( $\alpha = 0$ ) for which the initial calibration is performed. (b) compares the distortion correction results on the GPU without (left) and with (right) compensation of the lens rotation. (c), (d) and (e) present distortion correction results in various environments. All the results were obtained from a video sequence of 36 minutes with no system recalibration or reinitialization.

reference position ( $\alpha = 0$ ), enabling the determination of the matrix  $K_0$ , the RD parameter  $\xi$ , and the 3D coordinates of the grid points. Then, the camera head was carefully rotated without moving the lens probe in order to keep the relative pose with respect to the calibration pattern. The rotation center  $\mathbf{q}_i$  and the angular displacement  $\alpha_i$  were estimated for each frame using the geometry in Fig.8. Finally, the 3D grid points were projected onto the frame using equation 15, and the error distance to the actual image corner locations was measured. The red curve of Fig.9(b) shows the Root Mean Square (RMS) of the re-projection error for different angular displacements  $\alpha$ . The values vary between 2 and 5.6 pixels, but no systematic behavior can be observed. We believe that the reason for the errors is more in the experimental conditions than in the camera modeling. Since the images are very close range ( $\approx 10$  mm), a slight touch on the lens while rotating the camera head is enough to cause a re-projection error of several pixels. The results of Fig.9(a) not only validate the accuracy of the calibration, but show that having a model that accounts for the lens rotation is of key importance for achieving a correct compensation of the lens distortion.

The presented experiment only focused on the intrinsic parameters, while [1] and [2] consider both intrinsic and extrinsic calibration and employ additional instrumentation. Although no direct comparison can be made, it is worth mentioning that our reprojection error is smaller than [2] and equivalent to [1], where only points close to the image center were considered. From the above, and despite all conjectures, the experimental results clearly validate the proposed model.

## VI. RADIAL DISTORTION CORRECTION

This section discusses the rendering of the correct perspective images that are the final output of the visualization system. As pointed out in [23], the efficient warping of an image by a particular transformation should be performed using the inverse mapping method. Thus, we must derive the function  $\mathbf{F}$  that maps points  $\mathbf{y}$  in the desired undistorted image into points  $\mathbf{x}$  in the original distorted frame. From equation 15, it

follows that

$$\mathbf{F}(\mathbf{y}) \sim K_i \Gamma_\xi (R_{-\alpha_i, \mathbf{q}_i''} K_y^{-1} \mathbf{y}). \quad (18)$$

$K_y$  specifies certain characteristics of the undistorted image (e.g. center, resolution),  $R_{-\alpha_i, \mathbf{q}_i''}$  rotates the warping result back to the original orientation, and  $\mathbf{q}_i''$  is the back-projection of the rotation center  $\mathbf{q}_i$

$$\mathbf{q}_i'' \sim (q_{i,x}'' \quad q_{i,y}'' \quad 1)^T \sim \Gamma_\xi^{-1} (K_i^{-1} \mathbf{q}_i). \quad (19)$$

According to feedback from our medical partners, it is extremely important to preserve object's scale in the center region otherwise the practitioner may be reluctant to adopt the proposed visualization solution. So instead of correcting the RD and re-scaling the result to the resolution of the original frame we decided to expand the image periphery and keep the size of the undistorted center region, avoiding loss of information in the image center. This was done by computing the size  $u$  of the warped image from the radius of the boundary contour. Let  $r_d$  be the distance between the origin and the point  $K_i^{-1} \mathbf{p}_0$  (the distorted radius). The desired image size  $u$  is given by  $u = f r_u$ , where  $f$  is the camera focal length, and  $r_u$  is the undistorted radius determined using equation 8. Accordingly, the matrix  $K_y$  must be

$$K_y \sim \begin{pmatrix} f & 0 & -f q_{i,x}'' \\ 0 & f & -f q_{i,y}'' \\ 0 & 0 & 1 \end{pmatrix} \quad (20)$$

with the center of the warped image being the locus where the image rotation center  $\mathbf{q}_i$  is mapped. Note that a conjugation of extreme RD with a small original image resolution can produce pixelation in the periphery of the image. This effect is not noticeable when using high resolution input images. Anyway, in older systems this problem can be tackled by either improving the interpolation technique (currently we are using bilinear interpolation) or reducing the overall resolution of the target image. Fig.10 shows the RD correction results for some frames of a video sequence. The examples clearly show the improvements in the scene's perception, and the importance of taking into account the lens rotation during the correction of the image (Fig.10(b)).

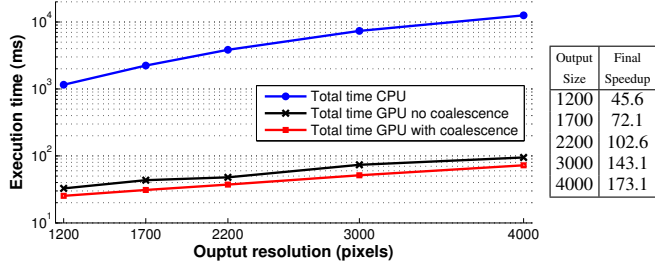


Fig. 11. Execution time per frame for various output image resolutions. The input images have a resolution of  $1600 \times 1200$  pixels and the output images have variable square size. The table on the right shows the speedup achieved with the optimized hybrid CPU+GPU approach relative to the CPU solution.

## VII. GPU IMPLEMENTATION AND TIME PROFILING

The rendering of warped images described in sections III and VI requires high performance computational resources to process data in real-time. In this section we describe the parallelization of our algorithms for correcting the RD on the GPU using the Compute Unified Device Architecture (CUDA) [24] interface. The natural parallelism underlying warping operations, where all data elements are computed by interpolating a common mapping function, and the efficient memory access procedure herein developed allow significant speedups. These turn out to be decisive in accomplishing the real-time requirements of the visualization application, especially when using HD input frames. We evaluate the impact of our hybrid CPU+GPU solution by comparing 3 approaches: (i) a purely CPU based solution running under an Intel® Core™2 Quad CPU; (ii) an unoptimized hybrid CPU+GPU version; and (iii) an optimized hybrid CPU+GPU version, both using a 8800 GTX GPU.

Fig.11 compares the execution times (required to process a single frame) achieved with the solutions mentioned above. The speedup table, a measure of how much faster the GPU is than the CPU, presents the ratio between the CPU and the optimized hybrid CPU+GPU execution times. The comparison given in Fig.11 shows that the CPU is not able to handle large warping operations (the most time consuming task of the algorithms) as efficiently as the GPU.

### A. Hybrid CPU+GPU solution

Fig.12 presents the optimized hybrid CPU+GPU implementation steps of the radial distortion correction algorithm and the details of the implementation strategy adopted in the development of the hybrid program to execute on the CPU and GPU. The parallelization of the algorithms on the GPU is divided into three main steps:

- **Image Conversions:** the image is divided into its RGB channels and a grayscale conversion is performed.
- **Boundary Estimation:** the grayscale image is bound to a texture [24] and the mapping to spherical coordinates (equation 2) along with the contour enhancement kernels are launched.
- **Radial Distortion Correction:** the 3 image channels, from the *Image Conversions* stage, are bound to textures and the RD correction kernel is launched.

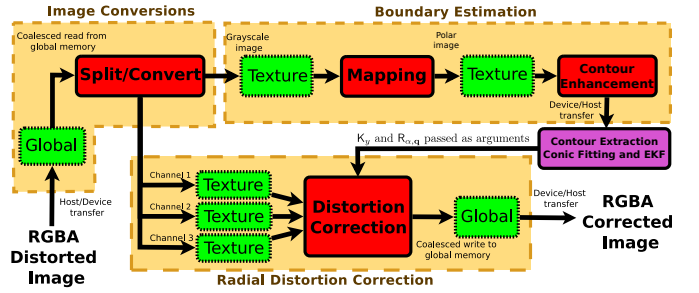


Fig. 12. Radial distortion correction algorithm steps. The red blocks represent CUDA kernels invocations. The green dotted blocks represent allocated device memory. Except for the purple block, which is computed on the CPU, all processing is performed on the GPU.

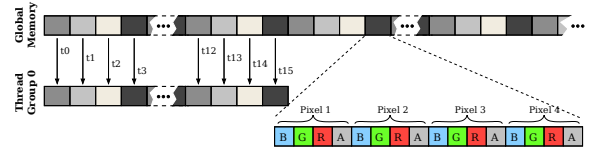


Fig. 13. Coalesced memory access by a group of threads ( $t_0$  to  $t_{15}$ ). Each channel (RGBA) of a pixel is represented using 8-bit precision.

There is an intermediary step (purple block in Fig. 12) that is computed in the CPU. Each line of the polar image is scanned for the contour points to which the ellipse is fitted. The ellipse parameters are fed to the EKF discussed in section V-B and the calibration parameters are updated and passed as arguments to the distortion correction kernel. This step is implemented on the CPU rather than the GPU because of the sequential nature of the processes involved.

The optimized hybrid CPU+GPU solution relies on a data pre-alignment procedure, that allows to perform a single memory access per group of threads (see Fig.13), which is known by *coalescence* [25], [26]. If the data to be processed by the GPU is misaligned instead, no coalesced accesses are performed and several memory transactions occur for each group of threads, reducing significantly the performance of the kernel under execution.

Although the *alpha* channel of the image is not being used, it is necessary to fulfill the memory layout requirement for performing fully coalesced accesses. An increase in the amount of data to be transferred introduces a penalty of 10.6% in the transfer time while the coalescence achieved reduces the kernels execution time by 66.1%. In sum, the coalesced implementation saves 38.7% of computational time relatively to the unoptimized hybrid CPU+GPU implementation.

### B. Time Profiling

Table II presents the time taken by each step in Fig.12 while processing a 150 frame video sequence (the times represent the mean time value of all frames processed for each resolution). By implementing coalesced accesses to global memory and exploiting the texture memory space of the GPU (optimized hybrid CPU+GPU solution) we were able to significantly shorten the execution time required to process a frame, compared with the other solutions presented in Fig.11.

TABLE II  
EXECUTION TIMES, IN MILLISECONDS, AND FRAMES PER SECOND (*fps*).

Input size	Output size	I.C.	B.E.	R.D.C.	Total	fps
640x480	700x700	2.53	3.48	2.51	<b>8.52</b>	<b>117</b>
640x480	1500x1500	2.51	3.15	7.92	<b>13.58</b>	<b>74</b>
1280x960	2000x2000	9.38	4.52	13.52	<b>27.41</b>	<b>36</b>
1280x960	3000x3000	9.37	5.36	28.21	<b>42.94</b>	<b>23</b>
1600x1200	2200x2200	11.86	5.02	17.22	<b>34.11</b>	<b>30</b>
1600x1200	4000x4000	11.72	4.88	51.39	<b>67.99</b>	<b>15</b>
2448x2048	3000x3000	30.27	11.89	32.07	<b>74.23</b>	<b>13</b>
2448x2048	5000x5000	30.17	12.46	79.88	<b>122.51</b>	<b>8</b>

Regarding the optimized hybrid CPU+GPU solution, whose processing times are given in table II, 4.8% to 15.0% of the total time is spent in CPU calculations (contour extraction, ellipse fitting and EKF for rotation center estimation), 41.4% to 61.1% is spent in data transfers to/from the host/device and 32.7% to 41.3% of the time is spent in the kernels' execution.

### VIII. CONCLUSION

The article proposes a versatile and low cost system for calibrating and correcting the RD in clinical endoscopy. The solution runs in real time in COTS hardware and takes into account usability constraints specific to medical procedures. Moreover, it can be used with any type of endoscopy technology, including oblique-viewing endoscopes and HD acquisition.

The development of the system led to new methods and models for the following problems: (i) intrinsic camera calibration in the OR with minimum user intervention; (ii) robust segmentation of the circular region; (iii) inference of the relative rotation between lens probe and camera-head using uniquely image information; and (iv) on-line updating of the camera calibration during the clinical procedure. In addition, we proposed an optimized hybrid CPU+GPU solution for the computation and this, along with carefully designed algorithms, makes it possible correct HD video inputs in real time. Furthermore, and since the approach is scalable, it will be suitable for execution on future GPU generations that are likely to have more cores. It will therefore easily support more complex processing or the processing of larger HD images.

The generation of correct perspectives of the scene in real time is likely to improve the depth perception of the surgeon. As future work, we intend to use this solution to quantify the influence of the RD in the success rate of surgeries. Moreover, the contributions of this work to endoscopic camera modeling and calibration are of major importance for applications in computer aided surgery and image guided intervention. Examples include improved visualization by image warping, 3D modeling and registration from endoscopic video, augmented reality and overlay of pre-operative information, visual SLAM for surgical navigation, etc.

### ACKNOWLEDGMENT

The authors would like to thank the Portuguese Agency for Innovation (ADI) that funded this research through the QREN co-promotion project n 2009/003512 sponsored by the Operational Program "Factores de Competitividade" and the European Fund for Regional Development. The system herein described is object of the provisional patent 20111000058190.

### REFERENCES

- [1] T. Yamaguchi *et al.*, "Camera Model and Calibration Procedure for Oblique-Viewing Endoscope," in *MICCAI*, 2003, pp. 373–381.
- [2] C. Wu, B. Jaramaz, and S. G. Narasimhan, "A Full Geometric and Photometric Calibration Method for Oblique-viewing Endoscope," *Int Journal of Computer Aided Surgery*, vol. 15, pp. 19–31, 2010.
- [3] N. Fukuda, Y. Chen, M. Nakamoto, and T., "A scope cylinder rotation tracking method for oblique-viewing endoscopes without attached sensing device," *Software Eng and Data Mining*, pp. 684–687, 2010.
- [4] R. I. Hartley and A. Zisserman, *Multiple View Geometry in Computer Vision*, 2nd ed. Cambridge University Press, ISBN: 0521540518, 2004.
- [5] K. Asari, S. Kumar, and D. Radhakrishnan, "A new approach for nonlinear distortion correction in endoscopic images based on least squares estimation," *IEEE Trans. Med. Imag.*, vol. 18, pp. 345–354, 1999.
- [6] J. Helferty, C. Zhang, G. McLennan, and W. Higgins, "Videoendoscopic distortion correction and its application to virtual guidance of endoscopy," *IEEE Trans. Med. Imag.*, vol. 20, pp. 605–617, 2001.
- [7] J. Barreto, J. Santos, P. Menezes, and F. Fonseca, "Ray-based Calibration of Rigid Medical Endoscopes," in *OMNIVIS*, 2008.
- [8] T. Stehle *et al.*, "Dynamic Distortion Correction for Endoscopy Systems with Exchangeable Optics," in *Bildverarbeitung für die Medizin*, Berlin, 2009, pp. 142–146.
- [9] J.-Y. Bouguet. Camera Calibration Toolbox for Matlab. [Online]. Available: [http://www.vision.caltech.edu/bouguetj/calib\\_doc/index.html#ref](http://www.vision.caltech.edu/bouguetj/calib_doc/index.html#ref)
- [10] Z. Zhang, "Flexible camera calibration by viewing a plane from unknown orientations," in *ICCV*, 1999, pp. 666–673.
- [11] R. Shahidi *et al.*, "Implementation, calibration and accuracy testing of an image-enhanced endoscopy system," *IEEE Trans. Med. Imag.*, vol. 21, pp. 1524–1535, Jan 2002.
- [12] C. Wengert, M. Reeff, P. Cattin, and G. Székely, "Fully automatic endoscope calibration for intraoperative use," in *Bildverarbeitung für die Medizin 2006*, 2006, pp. 419–423.
- [13] F. Vogt, S. Krüger, H. Niemann, and C. H. Schick, "A System for Real-Time Endoscopic Image Enhancement," in *MICCAI*, 2003, pp. 356–363.
- [14] S. Krüger *et al.*, "Evaluation of computer-assisted image enhancement in minimal invasive endoscopic surgery," *Methods Inf Med*, vol. 43, pp. 362–366, 2004.
- [15] J. Mallon and P. F. Whelan, "Which pattern? Biasing aspects of planar calibration patterns and detection methods," *Pattern Recognition Letters*, vol. 28, no. 8, pp. 921–930, Jan 2007.
- [16] J. Barreto, J. Roquette, P. Sturm, and F. Fonseca, "Automatic Camera Calibration Applied to Medical Endoscopy," in *BMVC*, 2009.
- [17] S. D. Buck, F. Maes, A. D'Hoore, and P. Suetens, "Evaluation of a novel calibration technique for optically tracked oblique laparoscopes," *MICCAI*, pp. 467–474, 2007.
- [18] Melo, R. and Barreto, João P. and Falcão, G., "Superior Visualization in Endoscopy," Tech. Rep., March 2011. [Online]. Available: <http://arthronav.isr.uc.pt/reports/visualizationreport.zip>
- [19] A. Fitzgibbon, M. Pilu, and R. Fisher, "Direct least square fitting of ellipses," *IEEE Trans. Pattern Anal. Mach. Intell.*, vol. 21, pp. 476–480, May 1999.
- [20] M. Fischler and R. Bolles, "Random Sample Consensus: A Paradigm for Model Fitting with Applications to Image Analysis and Automated Cartography," *Commun. ACM*, vol. 24, no. 6, pp. 381–395, 1981.
- [21] R. Hartley and S. B. Kang, "Parameter-free radial distortion correction with centre of distortion estimation," in *ICCV*, 2005, pp. 1834–1841.
- [22] S. M. Bozic, *Digital and Kalman Filtering*. Edward Arnold, 1979.
- [23] L. Velho, A. C. Frery, and J. Gomes, *Image Processing for Computer Graphics and Vision*. Springer, 2008.
- [24] *CUDA Programming Guide 3.0*, NVIDIA, February 2010, Rev 1.
- [25] D. Kirk and W.-m. Hwu, *Programming Massively Parallel Processors: A Hands-on Approach*. Morgan Kaufmann, 2010.
- [26] G. Falcao, L. Sousa, and V. Silva, "Massively LDPC Decoding on Multicore Architectures," *IEEE Trans. Parallel Distrib. Syst.*, vol. 22, pp. 309–322, 2011.